Numerical investigation of turbulence generation in non-breaking potential waves

Alexander V. Babanin[1] and Dmitry Chalikov[1,2]

Received 30 January 2012; revised 6 April 2012; accepted 18 April 2012; published 13 June 2012.

[1] Theoretically, potential waves cannot generate the vortex motion, but scale considerations indicate that if the steepness of waves is not too small, Reynolds number can exceed critical values. This means that in presence of initial non-potential disturbances the orbital velocities can generate the vortex motion and turbulence. In the paper, this problem was investigated numerically on basis of full two-dimensional (x-z) equations of potential motion with the free surface in cylindrical conformal coordinates. It was assumed that all variables are a sum of the 2D potential orbital velocities and 3D non-potential disturbances. The non-potential motion is described directly with 3D Euler equations, with very high resolution. The interaction between potential orbital velocities and non-potential components is accounted through additional terms which include the components of vorticity. Long-term numerical integration of the system of equations was done for different wave steepness. Vorticity and turbulence usually occur in vicinity of wave crests (where the velocity gradients reach their maximum) and then spread over upwind slope and downward. Specific feature of the wave turbulence at low steepness (steepness was kept low in order to avoid wave breaking) is its strong intermittency: the turbulent patches are mostly isolated and intermittency grows with decrease of wave amplitude. Maximum values of energy of turbulence are in agreement with available experimental data. The results suggest that even non-breaking potential waves can generate turbulence, which thus enhances the turbulence created by the shear current.

Citation: Babanin, A. V., and D. Chalikov (2012), Numerical investigation of turbulence generation in non-breaking potential waves, *J. Geophys. Res.*, *117*, C00J17, doi:10.1029/2012JC007929.

1. Introduction

[2] The concept of the wave-induced non-breaking turbulence was recently proposed by *Qiao et al.* [2004] and *Babanin* [2006] and then confirmed by measurements in the laboratory [*Babanin and Haus*, 2009, *Dai et al.*, 2010] and in the field [*Toffoli et al.*, 2011; A. Toffoli et al., The effect of wave-induced turbulence on the ocean mixed layer: Field observations on the Australian North-West Shelf, submitted to *Journal of Geophysical Research*, 2011]. *Dai et al.* [2010], for example, showed that, in presence of gently sloped non-breaking waves, initially stratified fluid became uniform by two orders of magnitude faster than in absence of the waves, that is in case of pure molecular diffusion. The experiment was supported by a one-dimensional turbulence-diffusion model which showed consistent results. Still, the mixing happened at the scale of thousands wave periods for such gentle and short waves. In this regard, experiment of *Beya et al.* [2012] should be mentioned, who reproduced the experimental setup of *Babanin and Haus* [2009] and used dye to see whether it will be dissolved due to wave turbulence over some 30 wave periods. It was not, but apparently for such short and small waves this cannot be expected.

[3] Essential importance of this turbulence for the dynamics of the upper ocean and for air-sea interactions in a broader sense has also been clearly demonstrated lately. In finite-depth environments and at the shelves, this turbulence produces mixing all the way to the bottom in response to a single storm, and this contribution is critical in adequate modeling of the sediment suspension [e.g., *Pleskachevsky et al.*, 2011]. When employed in ocean-circulation and general-circulation models, agreement between the modeling of sea-surface temperature and upper-ocean temperature profiles, and the data, improved by up to 35%, depending on wave climate at a particular location and on latitude [*Qiao et al.*, 2004, 2010; *Huang et al.*, 2008]. In modeling the current climate, account for such turbulence led to a significant increase of magnitudes of seasonal variation of main hydro-meteorological properties such as temperature, pressure, winds and precipitation [*Babanin et al.*, 2009].

[1] Centre for Ocean Engineering, Science and Technology, Swinburne University of Technology, Melbourne, Victoria, Australia.

[2] P. P. Shirshov Institute of Oceanology, Russian Academy of Sciences, Saint Petersburg, Russia.

Corresponding author: A. V. Babanin, Centre for Ocean Engineering, Science and Technology, Swinburne University of Technology, PO Box 218, Melbourne, Vic 3122, Australia. (ababanin@swin.edu.au)

[4] While the concept appears new and the wave-induced turbulence is missing from most of the ocean-mixing schemes, because the waves are routinely treated as irrotational and therefore not-generating turbulence, the idea was in fact well-familiar to oceanographers over 50 years ago. The book of *Kinsman* [1965] has a chapter on rotational wave motion, i.e., linear and nonlinear wave theory in presence of viscosity, with references to *Stokes* [1845], *Longuet-Higgins* [1953], *Phillips* [1961], and a section on wave-induced non-breaking turbulence. We should add *Kitaigorodskii* [1961] to this early list of papers.

[5] It is the success of potential theories of nonlinear waves, introduced in the 60s, which made the applications of non-potential wave theories seem redundant and eventually even led to them being nearly forgotten. Such theories certainly provide a rich range of useful physics, both deterministic and stochastic, i.e., for example, kinetic equation [*Hasselmann*, 1962; *Zakharov*, 1968; *Krasitskii*, 1994; *Janssen*, 2003; *Annenkov and Shrira*, 2006; *Zakharov*, 2010], modulational instability [*Zakharov*, 1966, 1967; *Benjamin and Feir*, 1967; *McLean*, 1982], Nonlinear Schrödinger Equation [*Benney and Newell*, 1967; *Zakharov*, 1967, 1968; *Dysthe*, 1979; *Stiassnie*, 1984; *Akhmediev and Korneev*, 1986; *Shemer and Dorfman*, 2008], Zakharov Equation [*Zakharov*, 1968; *Gramstad et al.*, 2011], Zakharov-Kolmogorov weak-turbulence solutions [*Zakharov and Filonenko*, 1966; *Zakharov and Zaslavskii*, 1982; *Badulin et al.*, 2007; *Gagnaire-Renou et al.*, 2011], Alber Equation [*Alber*, 1978; *Stiassnie et al.*, 2008], among others. In other respects, however, irrotational theories are inadequate. We will quote *Kinsman* [1965] on one such application:

> Careful measurements of the mass-transport velocity associated with waves… all suggest that the Stokes wave is unsatisfactory model so far as the mass-transport velocity associated with water waves is concerned. It would seem that the argument on which Stokes chose irrotationality was crucially unsound, if a study of water waves was his object… You do not arrive at the same place by setting the viscous terms to zero to begin with as you do if you retain them and then let the viscosity tend to zero at the end of your analysis.

[6] Another reason for the disrepute of the old rotational wave theories was a relatively small rate of production of vorticity within these approaches. Such low rates, however, were a consequence of the two-dimensionality of the old analytical solutions, and this issue was well-appreciated by the old school of oceanographers: “Unfortunately, the analysis of turbulence is very difficult, since the process is essentially three dimensional. This means that nothing remotely useful will result from a two-dimensional analysis of the sort we have used with infinitely long-crested waves” [*Kinsman*, 1965].

[7] This problem was later investigated by means of a linear-instability theory, and it was shown that this is not long-crestedness of the waves, but two-dimensionality of the turbulence which is the setback in 2D approaches. This instability problem was formulated first by *Benilov and Losovatskiy* [1977]. Later, the idea was further developed by *Kitaigorodskii and Lumley* [1983] and *Benilov et al.* [1993]. Within such theory, it was shown that pure two-dimensional motion remains potential because one-dimensional vortex (in vertical plane) does not interact with the wave orbital motion. If the turbulence is treated in three-dimensional sense, however, and the real turbulence is nearly always three-dimensional, the waves can generate the vortex in horizontal plane. Such vortex is unstable and further development of vorticity occurs due to exchange of energy between the components of vorticity. Then, due to nonlinearity, motion at smaller scales and more or less developed turbulent regime arise on behalf of the wave energy.

[8] Other theoretical and experimental studies should also be highlighted in this context, even if briefly. *Jacobs* [1978] introduced additional turbulent viscosity which remains after the mean orbital wave motion is averaged out, what *Pleskachevsky et al.* [2011] called the ‘symmetric effect’. *Anis and Moum* [1995], employed both the symmetric and ‘asymmetric’ effects, the latter being production of the turbulence due to waves being irrotational. In the field, the wave turbulence, unrelated to the breaking, was explicitly observed and even parameterized by *Yefimov and Khristoforov* [1971a, 1971b].

[9] Significance of such wave-induced turbulence, in the meantime, is hard to overestimate. The waves produce turbulence for the upper ocean in a number of ways, i.e., by breaking [e.g., *Chalikov and Belevich*, 1993], by interacting with background turbulence through the Stokes current [e.g., *Ardhuin and Jenkins*, 2006], through triggering Langmuir circulation [e.g., *Langmuir*, 1938; *McWilliams and Sullivan*, 2000] and through the wave orbital motion (see, e.g., *Babanin* [2011] for a review of these issues). While the former three mechanisms rely on downward diffusion or advection of the near-surface turbulence, the last one generates turbulence directly through the water column at the scale of the wavelength (100 m) if the associated Reynolds numbers (wave heights) are large enough.

[10] Thus, as have already been mentioned above, role of this turbulence in the upper-ocean mixing is very essential. It is interesting, however, to quote *Kinsman* [1965] also in the following regard: “… while the vorticity field induced by wave motion is of second order and affects the mean motion to second order, its effect on the fluctuating motion is of third order…” This is the order at which the potential-theory solutions for nonlinear wave interactions are obtained [e.g., *Hasselmann*, 1962], and therefore importance of the account of viscosity in fact can perhaps be extended much further.

[11] In the present paper, a new wave-turbulence model is discussed, results of its application are demonstrated and compared with experiment. This wave-turbulence model is based on full two-dimensional (x-z) equations of potential motion with the free surface in cylindrical conformal coordinates. These equations constitute a fully nonlinear model of 2D waves which is coupled with a 3D model for the turbulence. This latter non-potential motion is described directly with 3D Euler equations, with very high resolution. The interaction between potential orbital velocities and non-potential components is accounted through additional terms which include the components of vorticity. The effects of turbulence are incorporated with a use of subgrid turbulent energy evolution equation. The turbulent scale is assumed to be proportional to grid resolution (LES technique). The results suggest that even non-breaking potential waves can generate the turbulence, which thus enhances the turbulence created by the shear currents.

[12] In the paper, sections 2 through 5 are the description of different aspects of the model. Surface-following coordinates are introduced in section 2, followed by equations for vortical

motion in section 3. Section 4 describes LES approach employed for simulating the turbulence and section 5 the fully nonlinear wave model. Section 6 demonstrates computational results, and conclusions are formulated in final section 7.

2. Surface-Following Coordinates

[13] Let us introduce curvilinear surface-following conformal in plane ($x = x_1$, $y = x_2$) cylindrical coordinates (ξ, ϑ, ζ) connected with Cartesian coordinates (x, y, z) by relations (axis z is directed upward):

$$x = \xi + x_0(\tau) + \sum_{-M\le k<M, k\ne 0} sign(k)\,\eta_{-k}(\tau)\frac{\cosh|k|(\varsigma + H)}{\sinh|k|H}\theta_k(\xi), \tag{1a}$$

$$z = \zeta + \eta_0(\tau) + \sum_{-M\le k<M, k\ne 0} \eta_k(\tau)\frac{\sinh|k|(\varsigma + H)}{\sinh|k|H}\theta_k(\xi), \tag{1b}$$

$$y = \vartheta, \tag{1c}$$

$$t = \tau, \tag{1d}$$

where the factors containing hyperbolic functions allow us to introduce a finite depth $z = H$, k is wave number, M is a truncation parameter, t is time, η_k are Fourier amplitudes in presentation of the two-dimensional surface $\eta(\xi, \vartheta)$

$$\eta(\xi, \vartheta, \tau) = \sum_{-M\le k\le M} \eta_k(\tau)\theta_k(\xi), \tag{2}$$

and $\theta_k(\xi)$ denotes the function

$$\theta_k(\xi) = \begin{cases} \cos k\,\xi, & k \ge 0 \\ \sin k\,\xi, & k < 0 \end{cases}. \tag{3}$$

[14] The metric coefficients for transformation (1a), (1b), (1c), (1d) take the form

$$x_\xi = 1 + \sum_{-M\le k\le M} |k|h_k \frac{\cosh|k|(\zeta + H)}{\sin|k|H}\vartheta_k(\xi), \tag{4a}$$

$$z_\xi = -\sum_{-M\le k\le M} kh_{-k}\frac{\sinh|k|(\zeta + H)}{\sin|k|H}\vartheta_k(\xi), \tag{4b}$$

$$x_\tau = \sum_{-M\le k\le M} (h_\tau)_{-k}\frac{\cosh|k|(\zeta + H)}{\sin|k|H}\vartheta_k(\xi), \tag{4c}$$

$$z_\tau = \sum_{-M\le k\le M} sign(k)(h_\tau)_k\frac{\sinh|k|(\zeta + H)}{\sin|k|H}\vartheta_k(\xi). \tag{4d}$$

[15] Conformal coordinates satisfy the conditions:

$$\xi_x = \zeta_z = J^{-1}x_\xi = J^{-1}z_\zeta, \tag{5a}$$

$$\xi_z = -\zeta_x = -J^{-1}x_\zeta = J^{-1}z_\xi, \tag{5b}$$

$$\xi_t = J^{-1}\left(-z_\xi z_\tau - x_\xi x_\tau\right), \tag{5c}$$

$$\zeta_t = J^{-1}\left(z_\xi x_\tau - x_\xi z_\tau\right), \tag{5d}$$

$$\frac{\partial J}{\partial\tau} + \frac{\partial J\xi_t}{\partial\xi} + \frac{\partial J\zeta_t}{\partial\zeta} = 0, \tag{5e}$$

$$\frac{\partial J}{\partial\tau} + \frac{\partial}{\partial\xi}\left(-z_\xi z_\tau - x_\xi x_\tau\right) + \frac{\partial}{\partial\zeta}\left(z_\xi x_\tau - x_\xi z_\tau\right) = 0 \tag{5f}$$

where J is a Jacobian of transformation

$$J = x_\xi^2 + z_\xi^2. \tag{6}$$

[16] Note that all metric coefficients do not depend on coordinate ϑ. Below, rules of transformations are written out:

$$\frac{\partial()}{\partial x} = \xi_x\frac{\partial()}{\partial\xi} + \zeta_x\frac{\partial()}{\partial\zeta} = J^{-1}\left(x_\xi\frac{\partial()}{\partial\xi} - z_\xi\frac{\partial()}{\partial\zeta}\right) = J^{-1}\left(\frac{\partial()x_\xi}{\partial\xi} - \frac{\partial()z_\xi}{\partial\zeta}\right), \tag{7a}$$

$$\frac{\partial()}{\partial z} = \xi_z\frac{\partial()}{\partial\xi} + \zeta_z\frac{\partial()}{\partial\zeta} = J^{-1}\left(z_\xi\frac{\partial()}{\partial\xi} - x_\xi\frac{\partial()}{\partial\zeta}\right) = J^{-1}\left(\frac{\partial()z_\xi}{\partial\xi} - \frac{\partial()x_\xi}{\partial\zeta}\right), \tag{7b}$$

$$\frac{\partial()}{\partial t} = \frac{\partial()}{\partial\tau} + \xi_t\frac{\partial()}{\partial\xi} + \zeta_t\frac{\partial()}{\partial\zeta}. \tag{7c}$$

3. Equation for Vortical Motion

[17] Let us now consider Euler equation in the Gromeko-Lamb form

$$\frac{\partial\bar u}{\partial t} = -\frac{\partial}{\partial x}(\bar p + \bar E + z) + \bar\omega^y\bar w - \bar\omega^z\bar v, \tag{8a}$$

$$\frac{\partial\bar v}{\partial t} = -\frac{\partial}{\partial x}(\bar p + \bar E + z) + \bar\omega^z\bar u - \bar\omega^x\bar w, \tag{8b}$$

$$\frac{\partial\bar w}{\partial t} = -\frac{\partial}{\partial x}(\bar p + \bar E + z) + \bar\omega^x\bar v - \bar\omega^y\bar u, \tag{8c}$$

where $(\bar u, \bar v, \bar w)$ are full components of velocity, $\bar\omega^x, \bar\omega^y, \bar\omega^z$ are components of vorticity, $\bar p$ is a deviation of pressure from the hydrostatic pressure, $\bar E = 1/2 \cdot (\bar u^2 + \bar v^2 + \bar w^2)$ is kinetic energy. Since vorticity $\bar\Omega_i$ of potential flow is zero, analogous equation for potential motion described by variables (U, V, W, P) has the form

$$\frac{\partial \bar{U}}{\partial t} = -\frac{\partial}{\partial x}(\bar{P} + \bar{E} + z), \tag{9a}$$

$$\frac{\partial \bar{V}}{\partial t} = -\frac{\partial}{\partial y}(\bar{P} + \bar{E} + z), \tag{9b}$$

$$\frac{\partial \bar{W}}{\partial t} = -\frac{\partial}{\partial z}(\bar{P} + \bar{E} + z). \tag{9c}$$

[18] Full variables can be represented as a sum of vortical (u, v, w, p) and potential (U, V, W, P) components:

$$\begin{array}{l} \bar{u} = u + U, \quad \bar{v} = v, \quad \bar{w} = w + W, \\ \bar{p} = p + P, \quad \bar{\omega}^i = \omega^i + \Omega^i \quad \Omega^i = 0 \end{array} \tag{10}$$

and from (8a), (8b), (8c), it follows that

$$\frac{\partial u}{\partial t} = -\frac{\partial}{\partial x}(p + E + uU + wW + z) + \omega^y(w + W) - \omega^z v, \tag{11a}$$

$$\frac{\partial v}{\partial t} = -\frac{\partial}{\partial x}(p + E + uU + wW) + \omega^z(u + U) - \omega^x(w + W), \tag{11b}$$

$$\frac{\partial w}{\partial t} = -\frac{\partial}{\partial x}(p + E + uU + wW) + \omega^x v - \omega^y(u + U). \tag{11c}$$

[19] Converting (11a), (11b), (11c) to the standard form, we obtain

$$\frac{\partial u}{\partial t} + \frac{\partial uu}{\partial x} + \frac{\partial vu}{\partial y} + \frac{\partial wu}{\partial x} = -\frac{\partial}{\partial x}(p + uU + wW) + \omega^y W, \tag{12a}$$

$$\frac{\partial v}{\partial t} + \frac{\partial uv}{\partial x} + \frac{\partial vv}{\partial y} + \frac{\partial wv}{\partial x} = -\frac{\partial}{\partial y}(p + uU + wW) + \omega^z U - \omega^x W, \tag{12b}$$

$$\frac{\partial w}{\partial t} + \frac{\partial uw}{\partial x} + \frac{\partial vw}{\partial y} + \frac{\partial ww}{\partial x} = -\frac{\partial}{\partial z}(p + uU + wW) + \omega^y U. \tag{12c}$$

[20] Equations (12a), (12b), and (12c), together with continuity equation

$$\frac{\partial u}{\partial x} + \frac{\partial v}{\partial y} + \frac{\partial w}{\partial z} = 0, \tag{12d}$$

describe the fluid motion at low Reynolds numbers, provided velocity components (U, W) of potential motion are known. Solving these equations in presence of curvilinear interface is generally impossible, and these equations should be rewritten in surface-following coordinate system, in our case – cylindrical conformal coordinates. After such transformation, equations (12a), (12b), and (12c) take the form

$$\frac{dJu}{d\tau} = \omega^\vartheta W - x_\xi \textstyle\prod_\xi + z_\xi \prod_\xi + F_\xi, \tag{13a}$$

$$\frac{dJv}{d\tau} = \omega^\zeta U - \omega^\xi W - J \textstyle\prod_\vartheta + F_\vartheta, \tag{13b}$$

$$\frac{dJw}{d\tau} = -\omega^\vartheta U - z_\xi \textstyle\prod_\xi - x_\xi \prod_\zeta + F_\zeta. \tag{13c}$$

[21] Here ω^ξ, ω^ϑ, ω^ζ are vorticity components ω^x, ω^y, ω^z multiplied by Jacobian J, and Π is generalized pressure

$$\textstyle\prod = p + uU + wW + \frac{2}{3}e. \tag{14}$$

[22] Operator $\frac{d}{d\tau}$ in (13a), (13b), (13c) denotes the full temporal derivative

$$\frac{d()}{d\tau} = \frac{\partial()}{\partial\tau} + \frac{\partial()\hat{u}}{\partial\xi} + \frac{\partial()\hat{v}}{\partial\vartheta} + \frac{\partial()\hat{w}}{\partial\zeta} \tag{15}$$

where v is a lateral component of velocity and $(\hat{u}, \hat{w})$ are contravariant components of velocity defined by equations:

$$\hat{u} = \xi_t + J^{-1}\tilde{u}, \quad \hat{w} = \zeta_t + J^{-1}\tilde{w} \tag{16}$$

[23] Here, $(\hat{u}, \hat{v})$ are covariant velocity components

$$\tilde{u} = ux_\xi + wz_\xi, \quad \tilde{w} = -uz_\xi + wx_\xi, \tag{17}$$

connected with Cartesian velocity components (u, v) by relations:

$$u = J^{-1}\left(\hat{u}x_\xi - \hat{w}z_\xi\right), \quad w = J^{-1}\left(\hat{u}z_\xi + \hat{w}x_\xi\right). \tag{18}$$

[24] Components of vector ω^ξ, ω^ϑ, ω^ζ in curvilinear coordinates take the form

$$\omega^\xi = J\left(\frac{\partial w}{\partial y} - \frac{\partial v}{\partial z}\right) = J\frac{\partial w}{\partial y} - \frac{\partial z_\xi v}{\partial \xi} + \frac{\partial x_\xi v}{\partial \zeta}, \tag{19a}$$

$$\omega^\vartheta = J\left(\frac{\partial u}{\partial z} - \frac{\partial w}{\partial x}\right) = \frac{\partial z_\xi u}{\partial \xi} + \frac{\partial x_\xi u}{\partial \zeta} - \frac{\partial x_\xi w}{\partial \xi} + \frac{\partial z_\xi w}{\partial \zeta}, \tag{19b}$$

$$\omega^\zeta = J\left(\frac{\partial v}{\partial x} - \frac{\partial u}{\partial y}\right) = \frac{\partial x_\xi v}{\partial \xi} - \frac{\partial z_\xi v}{\partial \zeta} - J\frac{\partial u}{\partial y}. \tag{19c}$$

[25] Equation of continuity can be represented through the contravariant velocity components as

$$\frac{\partial J}{\partial \tau} + \frac{\partial J\hat{u}}{\partial \xi} + \frac{\partial Jv}{\partial \vartheta} + \frac{\partial J\hat{w}}{\partial \zeta} = 0 \tag{20}$$

and through covariant velocity components as

$$\frac{\partial \tilde{u}}{\partial \xi} + \frac{\partial v}{\partial \vartheta} + \frac{\partial \tilde{w}}{\partial \zeta} = 0. \tag{21}$$

[26] Equation (20) provides an accurate approximation of advection terms in (15), and continuity equation in form (21) served for derivation of Poisson equation for pressure. Let us represent equations (13a), (13b), and (13c) in the following form

$$\frac{\partial Ju}{\partial \tau} = -\left(x_\xi \prod_\xi - z_\xi \prod_\zeta\right) F^\zeta, \tag{22a}$$

$$\frac{\partial Jv}{\partial \tau} = -J\frac{\partial \prod}{\partial \vartheta} + F^\vartheta, \tag{22b}$$

$$\frac{\partial Jw}{\partial \tau} = -\left(z_\xi \prod_\xi + x_\xi \prod_\zeta\right) F^\zeta \tag{22c}$$

where (F^ξ, F^ϑ, F^ζ) are

$$F^\xi = -\frac{\partial Ju\tilde{u}}{\partial \xi} - \frac{\partial Juv}{\partial \vartheta} - \frac{\partial Ju\tilde{w}}{\partial \zeta} + J\omega^\vartheta W + T^\xi, \tag{23a}$$

$$F^\vartheta = -\frac{\partial Jv\tilde{u}}{\partial \xi} - \frac{\partial Jvv}{\partial \vartheta} - \frac{\partial Jv\tilde{w}}{\partial \zeta} + J\omega^\zeta U - J\omega^\xi W + T^\vartheta, \tag{23b}$$

$$F^\xi = -\frac{\partial Jw\tilde{u}}{\partial \xi} - \frac{\partial Jwv}{\partial \vartheta} - \frac{\partial Jw\tilde{w}}{\partial \zeta} - J\omega^\vartheta U + T^\zeta, \tag{23c}$$

and (T^ξ, T^ϑ, T^ζ) are the terms describing the turbulence

$$T^\xi = -\frac{\partial J\left(x_\xi \overline{u'u'} + z_\xi \overline{u'w'}\right)}{\partial \xi} - \frac{\partial \overline{u'v'}}{\partial \vartheta} - \frac{\partial J\left(-z_\xi \overline{u'u'} + x_\xi \overline{u'w'}\right)}{\partial \zeta}, \tag{24a}$$

$$T^\vartheta = -\frac{\partial J\left(x_\xi \overline{v'u'} + z_\xi \overline{v'w'}\right)}{\partial \xi} - \frac{\partial \overline{v'v'}}{\partial \vartheta} - \frac{\partial J\left(-z_\xi \overline{v'u'} + x_\xi \overline{v'w'}\right)}{\partial \zeta}, \tag{24b}$$

$$T^\zeta = -\frac{\partial J\left(x_\xi \overline{u'w'} + z_\xi \overline{w'w'}\right)}{\partial \xi} - \frac{\partial \overline{v'w'}}{\partial \vartheta} - \frac{\partial J\left(-z_\xi \overline{u'w'} + x_\xi \overline{w'w'}\right)}{\partial \zeta}. \tag{24c}$$

[27] The second-order turbulent moments are represented as follows

$$-\overline{u'u'} = 2K_m J^{-1}\Phi_{11} = 2K_m J^{-1}\left(\frac{\partial x_\xi u}{\partial \xi} - \frac{\partial z_\xi u}{\partial \zeta}\right), \tag{25a}$$

$$-\overline{u'v'} = K_m J^{-1}\Phi_{12} = K_m\left(\frac{\partial u}{\partial y} + J^{-1}\left(\frac{\partial x_\xi v}{\partial \xi} - \frac{\partial z_\xi v}{\partial \zeta}\right)\right), \tag{25b}$$

$$-\overline{u'w'} = K_m J^{-1}\Phi_{13} = K_m J^{-1}\left(\frac{\partial\left(u z_\xi + w x_\xi\right)}{\partial \xi} + \frac{\partial\left(u x_\xi - w z_\xi\right)}{\partial \zeta}\right), \tag{25c}$$

$$-\overline{v'v'} = 2K_m J^{-1}\Phi_{22} = 2K_m J^{-1}\frac{\partial v}{\partial y}, \tag{25d}$$

$$-\overline{v'w'} = K_m J^{-1}\Phi_{23} = K_m\left(\frac{\partial w}{\partial y} + J^{-1}\left(\frac{\partial z_\xi v}{\partial \xi} + \frac{\partial x_\xi v}{\partial \zeta}\right)\right), \tag{25e}$$

$$-\overline{w'w'} = 2K_m J^{-1}\Phi_{33} = 2K_m J^{-1}\left(\frac{\partial z_\xi w}{\partial \xi} + \frac{\partial x_\xi w}{\partial \zeta}\right). \tag{25f}$$

[28] Let us approximate the time derivative by the forward difference. Then, the new values of velocities (u^{t+1}, v^{t+1}, w^{t+1}) are defined by expressions

$$u^{t+1} = -\Delta\tau\left(J^{t+1}\right)^{-1}\left(x_\xi \prod_\xi - z_\xi \prod_\zeta\right) + \left(J^{t+1}\right)^{-1}\left(J^t u^t + \Delta\tau F^\xi\right), \tag{26a}$$

$$v^{t+1} = -\frac{\partial \prod}{\partial \vartheta} + \left(J^{t+1}\right)^{-1}\left(J^t v^t + \Delta\tau F^\vartheta\right), \tag{26b}$$

$$w^{t+1} = -\Delta\tau\left(J^{t+1}\right)^{-1}\left(z_\xi \prod_\xi + x_\xi \prod_\zeta\right) + \left(J^{t+1}\right)^{-1}\left(J^t w^t + \Delta\tau F^\zeta\right) \tag{26c}$$

where J^t and J^{t+1} are previous and new values of Jacobian. Equations (26a) and (26c) both contain gradients of pressure. For derivation of Poisson equation in curvilinear coordinates, we will transform the Cartesian velocity components into covariant velocity components using (17):

$$\tilde{u}^{t+1} = -\Delta\tau \prod_\xi + \Phi^\xi, \tag{27a}$$

$$v^{t+1} = -\Delta\tau \prod_\upsilon + \Phi^\vartheta, \tag{27b}$$

$$\tilde{w}^{t+1} = -\Delta\tau \prod_\zeta + \Phi^\zeta \tag{27c}$$

where (Φ^ξ, Φ^ϑ, Φ^ζ) are combinations of right-hand sides of equations (26a), (26b), and (26c).

[29] Now,

$$\frac{\partial \tilde{u}^{t+1}}{\partial \xi} + \frac{\partial v^{t+1}}{\partial \vartheta} + \frac{\partial \tilde{w}^{t+1}}{\partial \zeta} = 0 \tag{28}$$

and after substituting (27a), (27b), (27c) into (28), we obtain the Poisson equation for diagnostic calculation of pressure

$$\Delta \prod = (\Delta\tau)^{-1}\left((\Phi_u)_\xi + (\Phi_v)_\vartheta + (\Phi_w)_\vartheta\right). \tag{29}$$

[30] Hence, using the cylindrical conformal mapping allows us to obtain the standard scheme for calculation of generalized pressure (14). Equation (29) is solved in Fourier space with Three Diagonal Matrix Algorithm (TDMA). Equations (26a), (26b), and (26c) are solved by standard Fourier-Transform method. For approximation of vertical

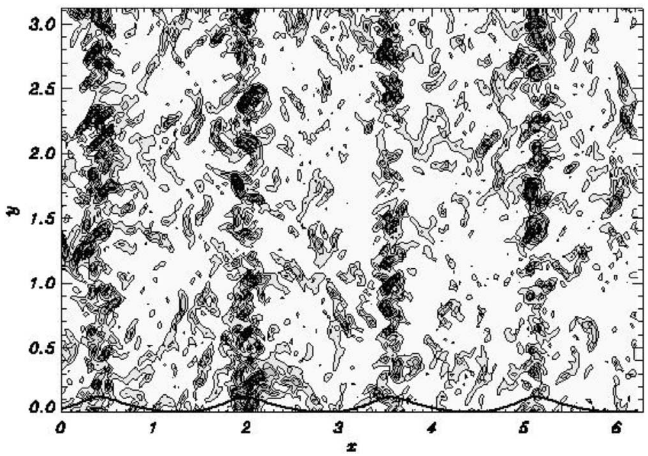

Figure 1. Distribution of energy $E_k = E_v + E_t$ in near-surface layer in relative units (top view, the vertical scale is the lateral direction). The black areas correspond approximately to 0.001 gH_s. At the bottom, the wave profile is indicated.

operators, the second order scheme was used. Equations (22a), (22b), and (22c) are solved with high resolution which allows us to reproduce directly the large-scale part of turbulence by means of the Large Eddy Simulations technique.

4. Large-Eddy Simulation Approach

[31] The LES approach imposes spatial filtering on instantaneous fields such that all flow structures bigger than the imposed filter scales are resolved, and smaller ones are filtered-out. Now, in order to compensate for these filtered-out scales, a subgrid turbulence model must be imposed in order to have correct representation of the original turbulent field. For LES approach to the near-wall modeling, different versions of modeling the subgrid turbulence contributions will be applied. Those include the classical [*Smagorinsky*, 1963] and dynamic [*Germano et al.*, 1991] approaches. Smagorinsky models as well as recently proposed coherent-structure scheme [*Kobayashi*, 2005] are schemes based on minimization of the theoretical subgrid dissipation [*Vreman*, 2004]. The turbulent boundary layer over a flat plate (with zero pressure gradient) was simulated by *Spalart* [1988] by employing DNS techniques over range of Reynolds numbers 225 < Re < 1410. For this particular case, a numerical database is provided (ERCOFTAC database) which makes it possible to perform very detailed comparison for first and second moments as well as for budgets of the second moments. In addition, effects of different numerical grid resolutions can be easily estimated and validation of LES results can be performed. More recently, *Porté-Agel et al.* [2000] proposed a scale-dependent dynamic subgrid-scale LES model. In contrast to the standard dynamic model, it does not rely on the assumption that the model coefficient is scale-variant. The new model introduces secondary test filter which, in addition to the standard test filter, is used to determine the model coefficient. The new model showed improvements of spectral slopes in the near-surface region where the standard Smagorinsky and standard dynamic model are either too dissipative or not dissipative enough, respectively. In order to demonstrate the applicability of the presented method to flows in non-orthogonal geometries, configurations with a wavy horizontal wall are selected next. This investigation are compared with DNS and LES results of *Kreltenauer and Schumann* [1992], *Tseng and Ferziger* [2004], and *Choi and Suzuki* [2005] and with experimental results of *Guenther and von Rohr* [2003] and Kruse *et al.* [2003].

[32] In the present work, the effects of subgrid turbulence are taken into account through coefficient of subgrid turbulent viscosity, which is used for calculations of second-order moments (25a)–(25f). The coefficient of turbulent viscosity is estimated with formula

$$K_{x,y} = C_s\left(J^{-1}\Delta\xi\Delta\vartheta\Delta\zeta\right)^{1/3} e^{1/2}, \quad C_s = 0.1, \tag{30}$$

where $l_t = (J^{-1}\Delta\xi\Delta\vartheta\Delta\zeta)^{1/3}$ is a turbulent length scale and e is kinetic energy of subgrid turbulence. The evolution of e is calculated with equation

$$\frac{dJe}{d\tau} = \frac{\partial}{\partial\xi}K_e\frac{\partial e}{\partial\xi} + \frac{\partial}{\partial\zeta}K_e\frac{\partial e}{\partial\zeta} + P - \varepsilon \tag{31}$$

where P is a rate of production of e and ε is dissipation rate, defined by relation

$$\varepsilon = C_D e^{3/2} l_t^{-1}. \tag{32}$$

[33] Expression for P is obtained from equations (25a)–(25f).

5. Model of Potential Waves

[34] The metric coefficients x_ξ, z_ξ and potential-velocity components U and W were calculated on basis of full potential equations which can be represented in the coordinates (1a), (1b) for $\zeta \le 0$ and the deep water as follows:

$$\Phi_{\xi\xi} + \Phi_{\zeta\zeta} = 0, \tag{33}$$

$$z_\tau = -x_\xi\xi_t - z_\xi\varsigma_t, \tag{34}$$

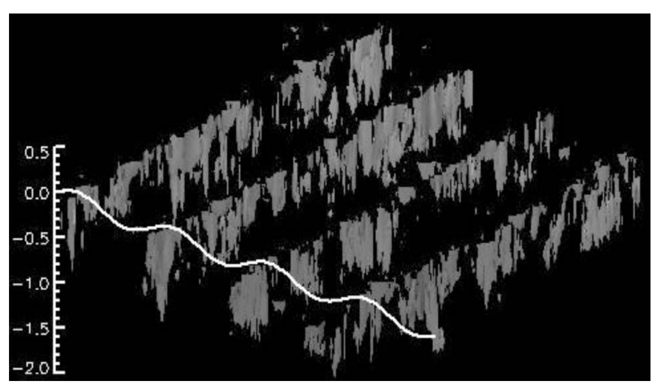

Figure 2. Volume distribution of energy $E_v = E_k + E_t$. Volume which corresponds to the 0.2 max(E_v) energy level is drawn. White line indicates the shape of long-crested waves.

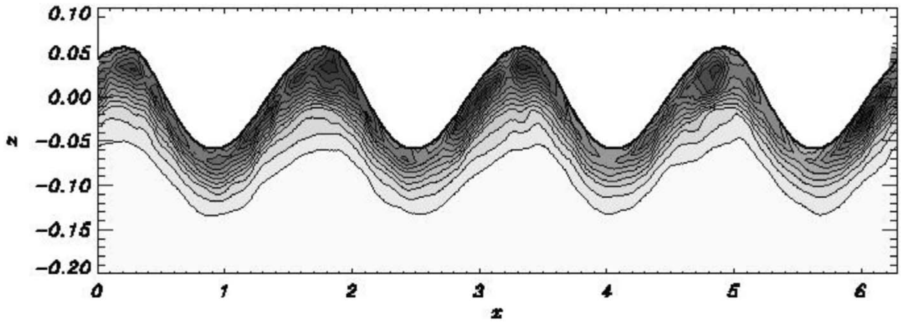

Figure 3. Distribution of energy $\overline{E_v}^y$ averaged over y-axis for the case of initially monochromatic waves with steepness ak = 0.24.

$$\varphi_\tau = -\zeta_t \varphi_\xi - \frac{1}{2} J^{-1}\left(\varphi_\xi^2 - \Phi_\zeta^2\right) - z - p_0, \tag{35}$$

where (34) and (35) are written for the surface $\zeta = 0$ (so that $z = \eta$, as represented by expansion (2)), p_0 is the surface pressure, J is the Jacobian, and ξ_τ and ς_τ are connected through the following relationship:

$$\zeta_t = -\left(J^{-1}\Phi_\zeta\right)_{\zeta=0}, \tag{36}$$

and $\varphi = \Phi(\zeta = 0)$.

[35] The capillarity was not taken into account in this investigation. The boundary condition assumes attenuation of the vertical velocity at depth:

$$\Phi_\zeta(\xi, \zeta \to -\infty, \tau) = 0. \tag{37}$$

[36] Solution of Laplace equation (33) with the boundary condition (35) is represented through the Fourier expansion, which reduces the system (33)–(35) to a 1D problem:

$$\Phi = \sum_{-M \le k \le M} \phi_k(\tau) \exp(k\zeta) \vartheta_k(\xi), \tag{38}$$

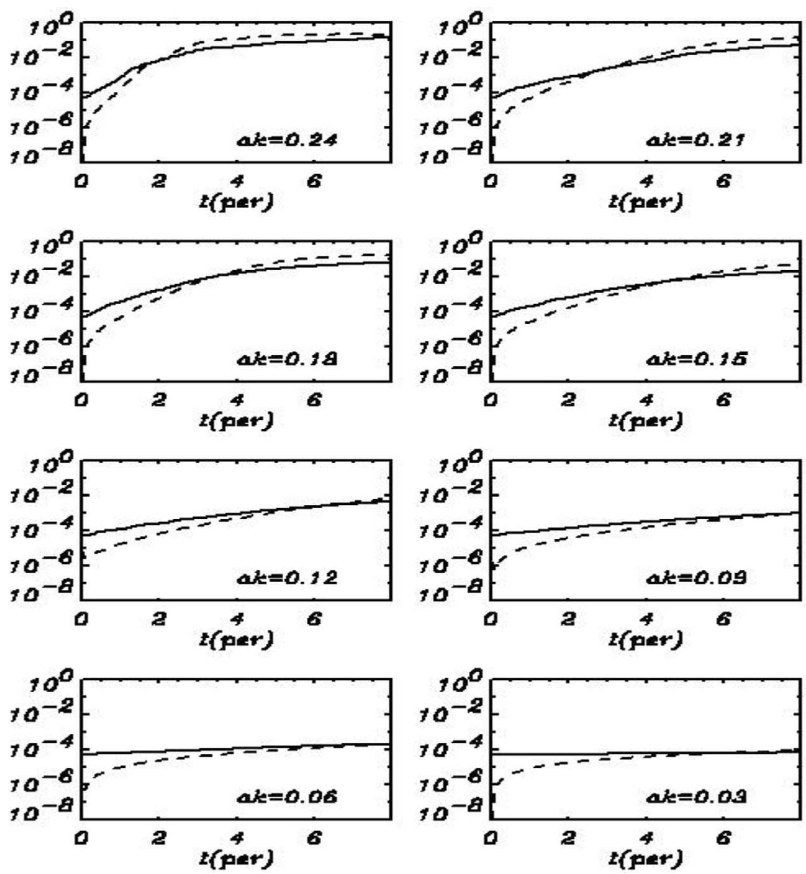

Figure 4. Evolution of volume-averaged kinetic energy of vortical motion $\overline{E_v}^{\xi\vartheta\zeta}$ (dashed line) and kinetic energy of subgrid turbulence (solid line) for initially monochromatic wave of different steepness (indicated as legend in each subplot).

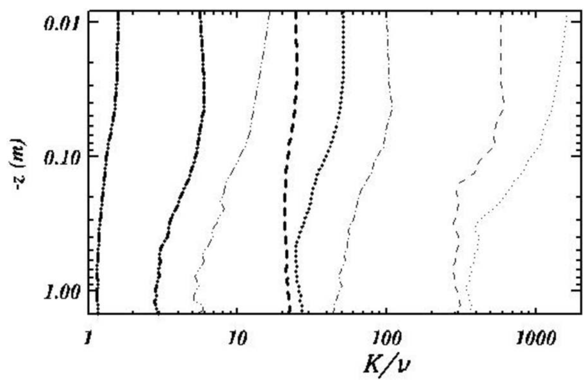

Figure 5. Vertical profiles of mixing coefficient $\tilde{K} = K/\nu$ under initially monochromatic waves for initial steepness ak = 0.24 (dotted curves), ak = 0.18 (dashed curves) and ak = 0.12 (dash-dotted curves), ak = 0.08 (dash-double-dotted curves). Thin lines correspond to maximum values of $\tilde{K}$ in the domain at each level, thick lines correspond to averaged values of $\tilde{K}$.

where ϕ_k are Fourier coefficients of the surface potential $\Phi(\xi, \zeta = 0, \tau)$. Equations (33)–(35) and (36) constitute a closed system of prognostic equations for the surface functions $z(\xi, \zeta = 0, \tau) = \eta(\xi, \tau)$ and the surface velocity potential $\Phi(\xi, \zeta = 0, \tau)$. For integration in time the fourth-order Runge-Kutta scheme was used, and selection of a suitable time step was done empirically. Details of the numerical scheme can be found in *Chalikov and Sheinin* [1998, 2005], *Chalikov* [2005, 2007, 2009], and *Chalikov and Rainchik* [2011]. Equations (33)–(35) were now integrated simultaneously with equations for vortical motions (24a), (24b), (24c). Components of potential velocity U and W were calculated using (37) and relations:

$$U = J^{-1}\left(x_\xi \Phi_\xi + z_\xi \Phi_\zeta\right), \tag{39}$$

$$W = J^{-1}\left(z_\xi \Phi_\xi + x_\xi \Phi_\zeta\right). \tag{40}$$

6. Results of Simulations

[37] The coupled waves/turbulence model was used first for simulation of generation of turbulence in a train of monochromatic waves with steepness $ak = 0.03 - 0.24$. The simulations were initially performed in a 2D version of model, when the lateral disturbances were absent. In this case, the imposed vortical motion was promptly dissipated, and turbulence did not develop. These features follow directly from equations (13a), (13b), and (13c), but such computations were still conducted for validation of the entire model.

[38] Figures in this section demonstrate outcomes of the 3D version. Initial conditions were assigned on a basis of linear theory as a train of harmonic waves with nondimensional wave number k_p = 4 (such setup corresponds to four waves in the domain). To be sure that the model is correct, the first simulations were done for purely potential flow in absence of non-potential disturbances. As expected, the vortical motion and turbulence were not generated. Other numerical experiments were then conducted with superimposed small random noise introduced as initial vortical velocity field. The waves remain two-dimensional, i.e., long-crested and do not change in the lateral y-direction. Note that monochromatic waves with steepness larger than 0.12 create new modes which finally result in disintegration of main modes and breaking. For the steepest wave with steepness ak = 0.24, breaking happens at periods which are still longer than those considered in the current work. Typical distribution of the sum E of the energy of explicitly simulated turbulent motion E_ν

$$E_\nu = \frac{1}{2}\left(u^2 + v^2 + w^2\right) \tag{41}$$

and the energy of subgrid turbulence E_t in a top layer with thickness of 0.01 L_p (L_p is wavelength) is shown in Figure 1. This is a view from above, and the curve at the bottom indicates the shape of the long-crested wave. As seen, the largest disturbances are concentrated along wave crests. These disturbances move with the phase velocity of carrying waves, which fact confirms that the dissipation time scale is small, and areas of increased vortical motion are tied with the zones of maximum gradients of orbital velocities.

[39] Figure 2 outlines shape of the volume below the water surface which corresponds to energy level of 0.2 max(E_ν). This figure demonstrates the volume distribution of the total energy of disturbances for the case ak = 0.24. White curve indicates the surface elevation, which is again the turbulent energy is concentrated along the long wave crests. For convenience, the vertical scales for energy and surface shape are chosen different.

[40] Distribution of y-averaged energy of wave-produced disturbances $\bar{E}^y$ is shown in Figure 3. As seen, the disturbances are concentrated near the surface and rapidly attenuate with depth. Such behavior is determined by properties of orbital velocity field: the squared Fourier components of velocity deformations (which are responsible for generation of vorticity) have their maxima at the surface and attenuate as exp(2kz) with the depth z negative if counted from surface.

[41] Time evolution of volume-averaged energy of explicitly simulated vortex motion and energy of turbulence $\overline{E_\nu}^{\xi\vartheta\zeta}$ are shown in Figure 4 (solid and dashed curves, respectively) for different steepness. As seen, both quantities grow with time and to the end of calculation reach more or less stationary conditions at time t = 6 periods. Further integration was not performed since we reproduced the exact conditions of laboratory experiments. The data on vertical distribution of turbulent viscosity coefficient normalized by molecular viscosity coefficient $\tilde{K} = K/\nu$ are given for waves with initial steepness ak = 0.24 (dotted curves), ak = 0.18 (dashed curves) and ak = 0.12 (dash-dotted curves) in Figure 5.

[42] Thin curves correspond to maximum values of $\tilde{K}$ in the domain at each level, thick curves correspond to averaged values of $\overline{\tilde{K}}^{\xi\vartheta}$. Maximum values of viscosity for all the three cases typically one decimal order of magnitude larger than averaged values, which fact points to large intermittency of horizontal distribution of turbulent viscosity. Note that for the case ak = 0.08 the average viscosity is very close

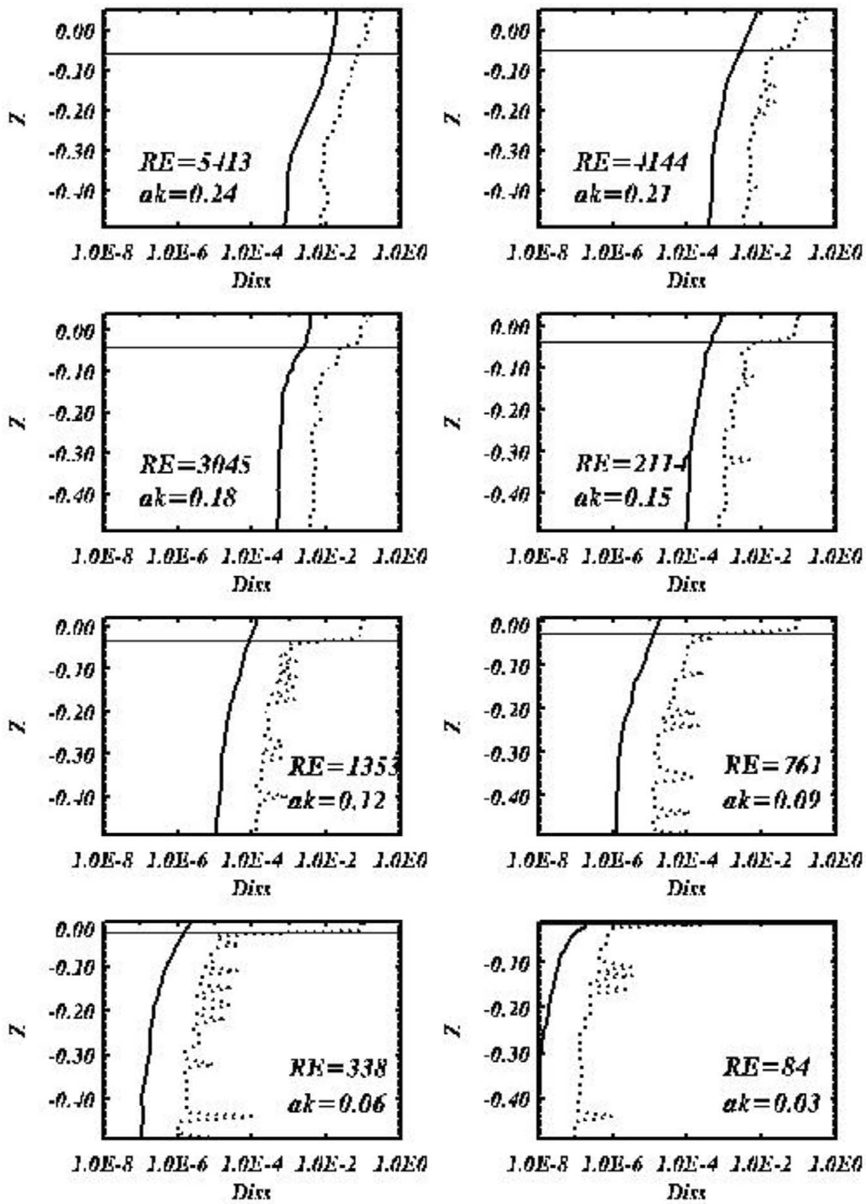

Figure 6. Vertical distribution of kinetic energy of the non-potential motion, average (solid line) and instantaneous maximal (dotted line), for a range of wave steepness from ak = 0.24 (top left corner) down to ak = 0.03 (bottom right corner), as shown in the legend of each subplot (*RE* is respective Reynolds numbers). The scales are dimensionless, the vertical scale is distance to the surface, the horizontal scale is the turbulence energy.

to molecular viscosity, this indicates that wave motion is laminar. However, even in this case, very narrow patches of turbulence in vicinity of wave peaks are still generated.

[43] In absence of breaking (that is for waves with small steepness and transitional Reynolds numbers) [see also *Babanin*, 2006], the turbulence in the model is strongly intermittent as seen in Figures 1–3, and it concentrates at the rear face of the waves. This is what was also observed in laboratory experiments of *Babanin and Haus* [2009] with such turbulence.

[44] The intermittence of turbulence is confirmed by vertical profiles, in Cartesian coordinates, of averaged and instantaneous maximal total energy E_v^{xy} (i.e., sum of energy of the vortical motion and energy of subgrid turbulence), shown in Figure 6. The records used for calculations were obtained toward the end of the 6th period of integration. Thin horizontal lines in these subplots correspond to the depths of wave troughs $z = \eta_{\min}$. Above this level, the averaging was done over the area occupied by the water. The dotted line indicates the maximum values observed at the 6th period of integration. Both curves suggest a considerable growth of the energy above wave troughs. As seen, the average values of energy are lower at least by a decimal order than their maximum values (see also Figure 1). Starting from the largest wave steepness, at the surface the kinetic energy is 10^{-2} and drops by two orders of magnitude at the

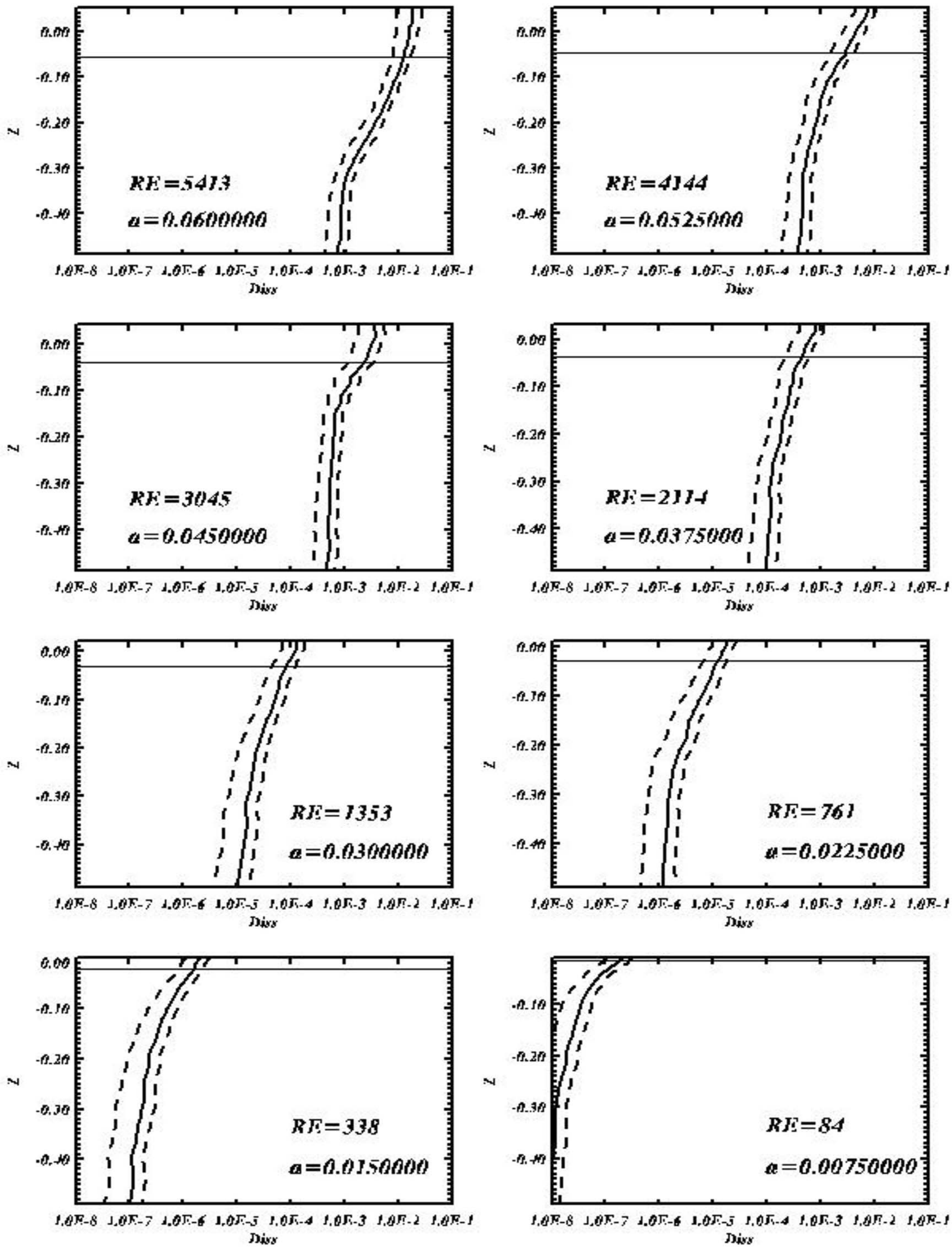

Figure 7. Vertical profiles of nondimensional rates of volumetric dissipation rate (m^2s^{-3}) for different steepness, as shown in the legend of each subplot (*a* is amplitude of 1.5 Hz waves, *RE* is respective Reynolds numbers). Solid curves correspond to average profiles and dashed curves indicate the variation. Figure is reproduced from *Babanin* [2011] (copyright Cambridge University Press, reprinted with permission).

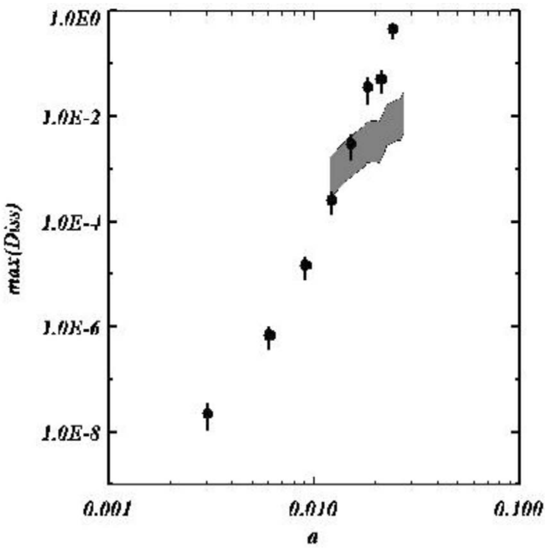

Figure 8. Maximal volumetric dissipation rates max*(Diss)* versus wave amplitude *a.* The shaded area corresponds to the range of measurement and scatter of the observational data of *Babanin and Haus* [2009]. Vertical segments indicate standard deviation of the dissipation estimates. Figure is reproduced from *Babanin* [2011] (copyright Cambridge University Press, reprinted with permission).

vertical scale of $\pi/8$, i.e., quarter of the wavelength, and then remains approximately constant. At the lower end of steepness, the surface energy is $\sim 10^{-7}$, and the two-order-of-magnitude drop occurs over 1/8th of wavelength vertical distance too. Thus, in the range of realistic water-wave steepness, intensity of the non-breaking wave-induced turbulence changes by 5 orders of magnitude. At $ak \sim 0.1$, the surface turbulence energy is $\sim 10^{-5}$. While such energy is apparently small as a dissipation source of the surface waves, it plays very essential role in the upper-ocean processes [*Qiao et al.*, 2004, 2010; *Huang et al.*, 2008; *Babanin et al.*, 2009], mixing of the stratified fluid [Dai *et al.*, 2010], sediment suspension in finite-depth seas [*Pleskachevsky et al.*, 2011], swell attenuation [*Babanin*, 2011], as described in section 1.

[45] Vertical profiles of nondimensional volumetric dissipation rate (solid curves) and its variance (dashed curves) obtained by averaging in Cartesian coordinate system are shown in Figure 7. Here, wavelength corresponds to frequency f = 1.5 Hz used in the laboratory experiment of *Babanin and Haus* [2009] and therefore amplitude *a* shown in the legend is an indicator of steepness. Different subplots show profiles for different wave amplitudes *a* and corresponding Wave Reynolds Numbers [*Babanin*, 2006]:

$$\mathrm{Re}_w = \frac{a^2\omega}{\nu} \tag{42}$$

denoted as *RE*, as indicated within these different panels. Here $a\omega$ signifies orbital velocity, i.e., the velocity scale in the Reynolds Number (ω is radian frequency), and v is kinematic viscosity of the water. It is quite obvious that due to intermittency the production of turbulence does not actually stop at low amplitudes/Re_w, but magnitude of the dissipation rates becomes so marginal ($\varepsilon \sim 10^{-8}$ m^2/s^3 at Re_w = 84) that it is hardly possible to measure. The lowest dissipation which *Babanin and Haus* [2009] were still able to detect above the noise level with their PIV method was of the order $\varepsilon \sim 10^{-4}$ m^2/s^3. If this is chosen as a reference, then $\mathrm{Re}_w \approx 2000$ can be regarded as the critical Wave Reynolds Number, close to the estimate $\mathrm{Re}_w \approx 3000$ of *Babanin* [2006].

[46] Comparison of the volumetric dissipation rates produced by the model and those measured by *Babanin and Haus* [2009] are given in Figure 8. Such dissipation rates max*(Diss)* are plotted as a function of dimensional wave amplitude *a(m)*, like volumetric dissipation rate ε (m^{2}s^{-3}) [*Babanin and Haus*, 2009, Figure 2]. It is, however, not exactly the same property as ε in *Babanin and Haus* [2009]. Those were measured below the troughs of the highest waves, i.e., always at some distance below the surface and even below the mean water level. Values of max*(Diss)* in Figure 8 indicate the maximum dissipation in the wave-induced-turbulence dissipation profile. In practice, this is an estimate of the volumetric dissipation rate near the surface and above the mean water level.

[47] Since the wave-induced turbulent energy is known to concentrate within wave crests [*Gemmrich*, 2010], it is expected that such max*(Diss)* should be greater than ε in *Babanin and Haus* [2009]. In the model, this happens because the generation of turbulence has maximum at the surface as mentioned above. In Figure 8, the shaded area corresponds to the range of measurements and scatter of the observational data of *Babanin and Haus* [2009]. There is quantitative agreement for wave amplitudes of $\sim$1.5 cm (wavelength here, as was in the experiment, corresponds to the frequency 1.5 Hz), and for the higher waves max*(Diss)* within the crests is greater than that measured below the troughs.

[48] Next set of calculations were done for initially assigned multimode wavefield corresponding to Pierson-Moskowitz spectrum. The size of domain in *x, y, z* directions was 1024 × 128 × 30 knots. The RMS steepness of this wavefield equals to 0.06, and explicit breaking events never happened. Some dissipation of wave energy occurs due to flux of energy into high wave number range, what was simulated through special algorithm [see *Chalikov and Sheinin*, 1998, 2005]. In order to keep the energy in wave system constant, the loss of energy was compensated by energy input from wind (details of such simulations can be

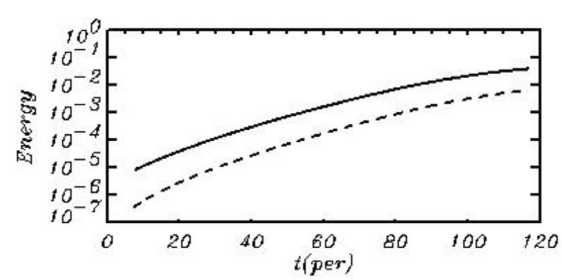

Figure 9. Evolution of volume-averaged turbulent kinetic energy E_k (solid curve) and energy of subgrid turbulence E_t (dashed curve). Both energies are normalized by the total wave energy and multiplied by length scale which is equal to 1.

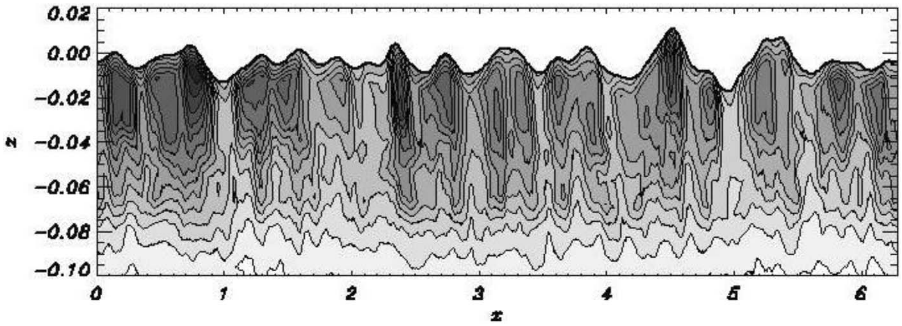

Figure 10. Distribution of averaged over y-axis energy $\overline{E_v}^y$ (nondimensional) for the case of waves with initially assigned Pierson-Moskowitz spectrum.

found, for example, in *Chalikov* [2009]). Initial modes were assigned, again, with small-amplitude theory, and energy of random noise was about 1% of wave energy.

[49] Temporal evolution of volume-averaged kinetic energy E_k (solid curve) and energy of subgrid turbulence E_t (dashed curve) during first 120 periods of integration is shown in Figure 9. As seen, both energies are growing with decreasing rate, and to the end of the integration period the energy is close to some quasi-stationary level.

[50] An example of y-averaged distribution of total energy $\overline{E_v}^y$ is given in Figure 10. Energy in Figure 10 is represented in nondimensional units. The turbulent kinetic energy and wave energy have different magnitudes, so in order to judge on absolute values of energy generated by potential waves it is reasonable to compare the integrated over depth total turbulent kinetic energy

$$E_v^{xyz} = \int_H^0 E_v^{xy} dz, \tag{43}$$

with total energy of waves equal to sum of potential and kinetic energy E_w [see *Chalikov and Sheinin*, 1998, 2005]. According to the current calculations, the total turbulent kinetic energy E_v^{xyz} is within the range (0.03–0.04)E_w. Hence, the energy of non-potential motion in fully developed waves is not small.

[51] The most important problem of wave-turbulence theory is the rate of wave energy dissipation (which on average is equal to production of non-potential energy P_v). The last numerical experiment with multimode wavefield gives a possibility to calculate this production rate of non-potential motion energy P_v on the basis of equations (22a), (22b), (22c), (23a), (23b), and (23c):

$$P_v = \left(\omega^\zeta u - \omega^\xi v\right) W + \left(\omega^\zeta v + \omega^\vartheta w\right) U \tag{44}$$

where (ω^ξ, ω^ϑ, ω^ζ) are components of vorticity in cylindrical conformal coordinates, (u, v, w) are velocity components of the vortical motion and (U, W) are components of the wave orbital velocity. Fortunately, when averaged over horizontal coordinates, these characteristics turned out to be essentially positive, otherwise the calculations could predict the inverse flux of energy from turbulence to potential waves, which is unlikely. The local profiles of averages over horizontal coordinates of production P_v^{xy}, as a function of nondimensional depth $\lambda = z/H_s$ for the last period of integration, are shown in Figure 11 (H_s is significant wave height, see (48)). These profiles are shown by gray lines and the mean profile P_v^{xy} by solid curve.

[52] Any estimation of Reynolds number (42) here gives values by orders magnitude exceeding the critical values of $Re \approx 2000 \div 3000$. It means that real wavefields should generate the fully developed turbulence, where a direct dependence of its intensity on Re number is absent. This is why the dependence of nondimensional variable P_v^{xy} on nondimensional depth can be approximated by a simple relation

$$\overline{P_v}^{xy} = 6.60 \cdot 10^{-8} \exp\left(17.47z + 6.76z^2\right). \tag{45}$$

[53] We should note that this parameterization is for the Pierson-Moscowitz spectrum, i.e., for fully developed waves. For developing waves, which are steeper, relative production of turbulence will be larger, but here such spectra were not modeled because steep waves also involve occasional breaking which was to be avoided in this study.

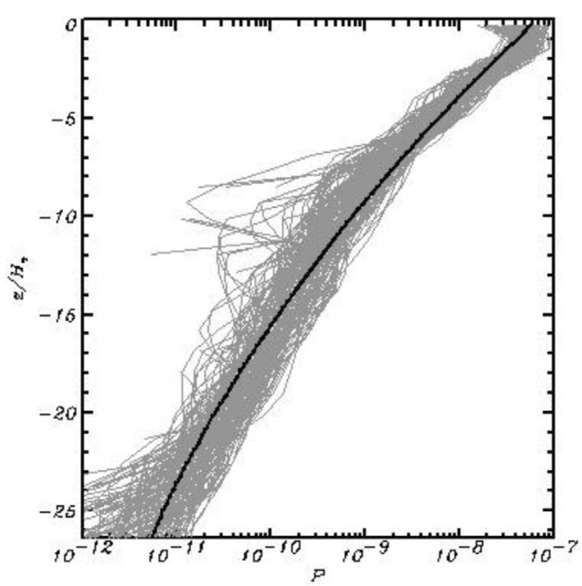

Figure 11. Vertical distribution of nondimensional dissipation rate P (see equation (46)) of the vortical motion as function of nondimensional depth $\tilde{z} = z/H_s$.

[54] Taking into account the scaling accepted in the current work, the dimensional rate of production $P(\mathrm{m^2 s^{-3}})$ can be represented as follows

$$H_s^{-1/2} g^{-3/2} P = 3.87 \cdot 10^{-7} \exp\left(0.506\tilde{z} + 0.0057\tilde{z}^2\right), \quad (46)$$

and we should remind that significant wave height H_s can be defined by integration over the wave spectrum

$$H_s = 4\left(\int_{\omega,\theta} S(\omega,\theta) d\omega d\theta\right)^{1/2}, \quad (47)$$

where ω is frequency and θ is angle.

[55] Dependence of type of (47) can be used for calculations of the volume input of energy from waves in the equation of turbulent energy evolution. Being integrated over depth, the equation gives the rate of dissipation of wave energy due to generation of turbulence.

7. Conclusions

[56] Numerical model for turbulence, unrelated to wave breaking and produced by orbital motion of potential waves is developed. The model consists of three parts: fully nonlinear potential model of two-dimensional (i.e., long-crested) waves, LES three-dimensional model based on full Reynolds equations with subgrid turbulence, three-dimensional model of evolution of subgrid turbulence. Three-dimensionality of the turbulence is of principle importance as the two-dimensional (in vertical plane) vortex does not interact with the wave orbital motion. The last two modules of the model are new and written in cylindrical conformal coordinates. Small perturbations of the potential motion are introduced and then allowed to develop as dictated by the theory.

[57] Long-term numerical integration of the system of equations was done for different wave steepness. The vorticity and turbulence usually occurs in vicinity of wave crests (where the velocity gradients reach their maximum) and then spreads over upwind slope and downward. If modeled at low wave steepness, which is necessary to avoid breaking, a specific feature of such wave turbulence is its strong intermittency: the turbulent patches are mostly isolated and intermittency grows with decrease of the wave amplitude. The maximum values of energy of turbulence are in agreement with available experimental data.

[58] The results suggest that even non-breaking potential waves can generate the turbulence, which thus enhances the turbulence created by the shear current or by breaking events. Importance of such turbulence has already been shown across a broad range of the upper-ocean processes, that is the upper-ocean mixing and circulation, sediment suspension in finite depths, swell attenuation, among others. The new model can be used to investigate the phenomenon in broad range of conditions and to produce parameterizations necessary in simulations which cannot reproduce the turbulence explicitly. The wave-turbulence model can be used for qualitative and even quantitative investigation of the phenomenon.

[59] **Acknowledgments.** This research is supported through Australian Research Council grants DP1093517, DP1093349 and LP0883888 (co-sponsored by Woodside Energy Ltd) and grant N00014-101-0418 of the U.S. Office of Naval Research (co-sponsored by NOAA and U.S. Army Corps).

References

Akhmediev, N. N., and V. I. Korneev (1986), Modulational instability and periodic solutions of the nonlinear Schrödinger equation, *Teor. Mat. Fiz.*, *69*, 189–194.

Alber, I. E. (1978), The effects of randomness on the stability of two-dimensional wavetrains, *Proc. R. Soc. London, Ser. A*, *363*, 525–546, doi:10.1098/rspa.1978.0181.

Anis, A., and J. N. Moum (1995), Surface wave-turbulence interactions: Scaling $\varepsilon(z)$ near the surface, *J. Phys. Oceanogr.*, *25*, 2025–2045, doi:10.1175/1520-0485(1995)025<2025:SWISNT>2.0.CO;2.

Annenkov, S. Y., and V. I. Shrira (2006), Role of non-resonant interactions in evolution of nonlinear random water wave fields, *J. Fluid Mech.*, *561*, 181–207, doi:10.1017/S0022112006000632.

Ardhuin, F., and A. D. Jenkins (2006), On the interaction of surface waves and upper ocean turbulence, *J. Phys. Oceanogr.*, *36*, 551–557, doi:10.1175/JPO2862.1.

Babanin, A. V. (2006), On a wave-induced turbulence and a wave-mixed upper ocean layer, *Geophys. Res. Lett.*, *33*, L20605, doi:10.1029/2006GL027308.

Babanin, A. V. (2011), *Breaking and Dissipation of Ocean Surface Waves*, 480 pp., Cambridge Univ. Press, Cambridge, U. K., doi:10.1017/CBO9780511736162.

Babanin, A. V., and B. K. Haus (2009), On the existence of water turbulence induced by non-breaking surface waves, *J. Phys. Oceanogr.*, *39*, 2675–2679, doi:10.1175/2009JPO4202.1.

Babanin, A. V., A. Ganopolski, and W. R. C. Phillips (2009), Wave-induced upper-ocean mixing in a climate modelling of intermediate complexity, *Ocean Modell.*, *29*, 189–197, doi:10.1016/j.ocemod.2009.04.003.

Badulin, S. I., A. V. Babanin, V. E. Zakharov, and D. Resio (2007), Weakly turbulent laws of wind-wave growth, *J. Fluid Mech.*, *591*, 339–378, doi:10.1017/S0022112007008282.

Benilov, A. Y., and Y. Lozovatskiy (1977), Semi-empirical methods of the turbulence description in the ocean, in *The Turbulent Diffusion of the Ingredients in the Sea*, *Inf. Bull. 5*, pp. 89–97, Coord. Cent., Counc. for Mutual Econ. Assistance, Moscow.

Benilov, A. Y., T. G. McKee, and A. S. Safray (1993), On the vortex instability of the linear surface wave, in *Numerical Methods in Laminar and Turbulent Flow*, vol. 8, part 2, edited by C. Taylor, pp. 1323–1334, Pineridge, Swansea, U. K.

Benjamin, T. B., and J. E. Feir (1967), The disintegration of wave trains in deep water. Part 1. Theory, *J. Fluid Mech.*, *27*, 417–430, doi:10.1017/S002211206700045X.

Benney, D. J., and A. C. Newell (1967), The propagation of nonlinear wave envelopes, *J. Math. Phys.*, *46*, 133–139.

Beya, J. F., W. L. Peirson, and M. L. Banner (2012), Turbulence beneath finite amplitude water waves, *Exp. Fluids*, *52*, 1319–1330.

Chalikov, D. (2005), Statistical properties of nonlinear one-dimensional wave fields, *Nonlinear Processes Geophys.*, *12*, 671–689, doi:10.5194/npg-12-671-2005.

Chalikov, D. (2007), Numerical simulation of Benjamin-Feir instability and its consequences, *Phys. Fluids*, *19*, 016602, doi:10.1063/1.2432303.

Chalikov, D. (2009), Freak waves: Their occurrence and probability, *Phys. Fluids*, *21*, 076602, doi:10.1063/1.3175713.

Chalikov, D., and M. Belevich (1993), One-dimensional theory of the wave boundary layer, *Boundary Layer Meteorol.*, *63*, 65–96, doi:10.1007/BF00705377.

Chalikov, D., and S. Rainchik (2011), Coupled numerical modelling of wind and waves and theory of the wave boundary layer, *Boundary Layer Meteorol.*, *138*, 1–41, doi:10.1007/s10546-010-9543-7.

Chalikov, D., and D. Sheinin (1998), Direct modeling of one-dimensional nonlinear potential waves, *Adv. Fluid Mech.*, *17*, 207–258.

Chalikov, D., and D. Sheinin (2005), Modeling of extreme waves based on equations of potential flow with a free surface, *J. Comput. Phys.*, *210*, 247–273, doi:10.1016/j.jcp.2005.04.008.

Choi, H. S., and K. Suzuki (2005), Large eddy simulation of turbulent flow and heat transfer in a channel with one wavy wall, *Int. J. Heat Fluid Flow*, *26*, 681–694, doi:10.1016/j.ijheatfluidflow.2005.03.001.

Dai, D., F. Qiao, W. Sulisz, L. Han, and A. V. Babanin (2010), An experiment on the non-breaking surface-wave-induced vertical mixing, *J. Phys. Oceanogr.*, *40*, 2180–2188, doi:10.1175/2010JPO4378.1.

Dysthe, K. B. (1979), Note on a modification to the nonlinear Schrödinger equation for application to deep water waves, *Proc. R. Soc. London, Ser. A*, *369*, 105–114.

Gagnaire-Renou, E., M. Benoit, and S. I. Badulin (2011), On weakly turbulent scaling of wind sea in simulations of fetch-limited growth, *J. Fluid Mech.*, *669*, 178–213, doi:10.1017/S0022112010004921.

Gemmrich, J. (2010), Strong turbulence in the wave crest region, *J. Phys. Oceanogr.*, *40*, 583–595, doi:10.1175/2009JPO4179.1.

Germano, M., U. Piomelli, P. Moin, and W. Cabot (1991), A dynamic subgrid-scale eddy-viscosity model, *Phys. Fluids A*, *3*, 1760–1765, doi:10.1063/1.857955.

Gramstad, O., Y. Agnon, and M. Stiassnie (2011), Localized Zakharov equation; derivation and validation, *Eur. J. Mech. B*, *30*, 137–146, doi:10.1016/j.euromechflu.2010.10.004.

Guenther, A., and R. von Rohr (2003), Large-scale structures in a developed flow over a wavy wall, *J. Fluid Mech.*, *478*, 257–285.

Hasselmann, K. (1962), On the non-linear energy transfer in a gravity-wave spectrum. Part I. General theory, *J. Fluid Mech.*, *12*, 481–500, doi:10.1017/S0022112062000373.

Huang, C., F. Qiao, and Z. Song (2008), The effect of the wave-induced mixing on the upper ocean temperature in a climate model, *Acta Oceanol. Sin.*, *27*, 104–111.

Jacobs, C. A. (1978), Numerical simulations of the natural variability in water temperature during BOMEX using alternative forms of the vertical eddy exchange coefficient, *J. Phys. Oceanogr.*, *8*, 119–141, doi:10.1175/1520-0485(1978)008<0119:NSOTNV>2.0.CO;2.

Janssen, P. A. E. M. (2003), Nonlinear four-wave interaction and freak waves, *J. Phys. Oceanogr.*, *33*, 863–884, doi:10.1175/1520-0485(2003)33<863:NFIAFW>2.0.CO;2.

Kinsman, B. (1965), *Wind Waves: Their Generation and Propagation on the Ocean Surface*, 676 pp., Prentice Hall, Englewood Cliffs, N. J.

Kitaigorodskii, S. A. (1961), On the possibility of theoretical calculation of vertical temperature profile in upper layer of the sea, *Bull. Acad. Sci. USSR Geophys. Ser.*, *3*, 313–318.

Kitaigorodskii, S. A., and J. L. Lumley (1983), Wave-turbulence interaction in the upper ocean. Part 1: The energy balance of the interacting fields of surface wind waves and wind-induced three-dimensional turbulence, *J. Phys. Oceanogr.*, *13*, 1977–1987, doi:10.1175/1520-0485(1983)013<1977:WTIITU>2.0.CO;2.

Kobayashi, H. (2005), The subgrid-scale models based on coherent structures for rotating homogeneous turbulence and turbulent channel flow, *Phys. Fluids*, *17*, 045104.

Krasitskii, V. P. (1994), On reduced equations in the Hamiltonian theory of weakly nonlinear surface waves, *J. Fluid Mech.*, *272*, 1–20, doi:10.1017/S0022112094004350.

Kreltenauer, K., and U. Schumann (1992), Numerical simulation of turbulent convection over wavy terrain, *J. Fluid Mech.*, *237*, 261–299, doi:10.1017/S0022112092003410.

Kruse, N., A. Guenther, and R. von Rohr (2003), Dynamics of large-scale structures in turbulent flow over a wavy wall, *J. Fluid Mech.*, *485*, 87–96, doi:10.1017/S0022112003004439.

Langmuir, I. (1938), Surface motion of water induced by the wind, *Science*, *87*, 119–123, doi:10.1126/science.87.2250.119.

Longuet-Higgins, M. S. (1953), Mass transport in water waves, *Philis. Trans. R. Soc. A*, *245*, 535–581, doi:10.1098/rsta.1953.0006.

McLean, J. W. (1982), Instabilities of finite-amplitude water waves, *J. Fluid Mech.*, *114*, 315–330, doi:10.1017/S0022112082000172.

McWilliams, J. C., and P. P. Sullivan (2000), Vertical mixing by Langmuir circulations, *Spill Sci. Technol. Bull.*, *6*, 225–237, doi:10.1016/S1353-2561(01)00041-X.

Phillips, O. M. (1961), A note on the turbulence generated by gravity waves, *J. Geophys. Res.*, *66*, 2889–2893, doi:10.1029/JZ066i009p02889.

Pleskachevsky, A., M. Dobrynin, A. V. Babanin, H. Gunther, and E. Stanev (2011), Turbulent diffusion due to ocean surface waves indicated by suspended particulate matter. Implementation of satellite data into numerical modelling, *J. Phys. Oceanogr.*, *41*, 708–724, doi:10.1175/2010JPO4328.1.

Porté-Agel, F., C. Meneveau, and M. B. Parlange (2000), A scale-dependent dynamic model for large-eddy simulation: Application to a neutral atmospheric boundary layer, *J. Fluid Mech.*, *415*, 261–284, doi:10.1017/S0022112000008776.

Qiao, F., Y. Yeli, Y. Yang, Q. Zheng, C. Xia, and J. Ma (2004), Wave-induce mixing in the upper ocean: Distribution and application to a global ocean circulation model, *Geophys. Res. Lett.*, *31*, L11303, doi:10.1029/2004GL019824.

Qiao, F., Y. Yuan, T. Ezer, C. Xia, Y. Yang, X. Lu, and Z. Song (2010), A three-dimensional surface wave-ocean circulation coupled model and its initial testing, *Ocean Dyn.*, *60*, 1339–1355, doi:10.1007/s10236-010-0326-y.

Shemer, L., and B. Dorfman (2008), Spatial vs. temporal evolution of nonlinear wave groups - experiments and modeling based on the Dysthe equation, paper presented at 27th International Conference on Offshore Mechanics and Arctic Engineering, Am. Soc. of Mech. Eng., Estoril, Portugal, 15–20 June.

Smagorinsky, J. (1963), General circulation experiments with the primitive equations I. The basic experiment, *Mon. Weather Rev.*, *91*, 99–164, doi:10.1175/1520-0493(1963)091<0099:GCEWTP>2.3.CO;2.

Spalart, P. R. (1988), Direct simulation of a turbulent boundary layer up to $Re_\theta = 1410$, *J. Fluid Mech.*, *187*, 61–83, doi:10.1017/S0022112088000345.

Stiassnie, M. (1984), Note on the modified nonlinear Schrodinger equation for deep water waves, *Water Motion*, *6*, 431–433, doi:10.1016/0165-2125(84)90043-X.

Stiassnie, M., A. Regev, and Y. Agnon (2008), Recurrent solution of Alber's equation for random water-wave fields, *J. Fluid Mech.*, *598*, 245–266, doi:10.1017/S0022112007009998.

Stokes, G. G. (1845), On the theories of the internal friction of fluids in motion, and on the equilibrium and motion of elastic solids, *Trans. Cambridge Philos. Soc.*, *8*, 287–305.

Toffoli, A., A. Babanin, and J. McConochie (2011), Field observations of the mixed-layer depth in the Indian Ocean: Effect of wave-induced turbulence, paper presented at General Assembly 2011, Eur. Geosci. Union, Vienna, 3–8 April.

Tseng, Y. H., and J. H. Ferziger (2004), Large-eddy simulation of turbulent wavy boundary flow—Illustration of vortex dynamics, *J. Turbul.*, *5*, N34, doi:10.1088/1468-5248/5/1/034.

Vreman, A. W. (2004), An eddy-viscosity subgrid-scale model for turbulent shear flow: Algebraic theory and applications, *Phys. Fluids*, *16*, 3670–3681, doi:10.1063/1.1785131.

Yefimov, V. V., and G. N. Khristoforov (1971a), Wave-related and turbulent components of velocity spectrum in the top sea layer, *Izv. Russ. Acad. Sci. Atmos. Oceanic Phys., Engl. Transl.*, *7*, 200–211.

Yefimov, V. V., and G. N. Khristoforov (1971b), Spectra and statistical relations between the velocity fluctuations in the upper layer of the sea and surface waves, *Izv. Russ. Acad. Sci. Atmos. Oceanic Phys., Engl. Transl.*, *7*, 1290–1310.

Zakharov, V. E. (1966), The instability of waves in nonlinear dispersive media [in Russian], *Zh. Eksp. Teor. Fiz. Pis'ma Red.*, *51*, 1107–1114.

Zakharov, V. E. (1967), The instability of waves in nonlinear dispersive media, *Sov. Phys. JETP, Engl. Transl.*, *24*, 740–744.

Zakharov, V. E. (1968), Stability of periodic waves of finite amplitude on the surface of deep fluid, *J. Appl. Mech. Tech. Phys., Engl. Transl.*, *2*, 190–194.

Zakharov, V. E. (2010), Energy balance in a wind-driven sea, *Phys. Scr. T.*, *142*, 014052.

Zakharov, V. E., and N. N. Filonenko (1966), The energy spectrum for stochastic oscillation of a fluid's surface, *Dokl. Acad. Nauk SSSR, Engl. Transl.*, *170*, 1992–1995.

Zakharov, V. E., and M. M. Zaslavskii (1982), Kinetic equation and Kolmogorov's spectra in a weak turbulence theory of wind waves [in Russian with English abstract], *Izv. Akad. Nauk SSSR, Ser. Fiz. Atmos. Okeana*, *18*, 970–979.